Optimal Spectral Topography and Its Effect on Model Climate

MARK HOLZER

Canadian Centre for Climate Modelling and Analysis, Atmospheric Environment Service, University of Victoria,
Victoria, British Columbia, Canada

ABSTRACT

Gibbs oscillations in the truncated spectral representation of the earth's topography are strongly reduced by determining its spectral coefficients as a minimum of a nonuniformly weighted, nonquadratic cost function. The cost function penalizes the difference between spectral and true topography with weights that are explicit functions of the topographic height and its gradient. The sensitivity of the Canadian Climate Centre general circulation model's climate to the presence of Gibbs oscillations is determined for T32 and T48 resolutions by comparing the climates with optimal spectral topography to those with standard spectral topography. The main effect of Gibbs oscillations in the standard spectral topography is to induce spurious grid-scale ripples in the surface fluxes, which, for the surface energy balance, can be on the order of several tens of watts per square meter. Ripples in the surface fluxes are nearly absent in the model climate with the optimal spectral topography.

1. Introduction

For general circulation models (GCMs) with spectral dynamics, the lower boundary provided by the topography must also be represented spectrally. Unfortunately, the truncated spectral expansion of the topographic height (referred to here as the spectral topography) suffers from Gibbs oscillations in real space that induce spurious ripples in the surface fields. Gibbs oscillations are a consequence of the nonuniform convergence of spectral expansions at jump discontinuities (see, e.g., Morse and Feshbach 1953). Thus, Gibbs oscillations occur where the earth's topography has sharp gradients such as, for example, where the Andes plunge into the Pacific and the Himalayas erupt from the Ganges plain.

The fundamental reason why the standard spectral representation of the topography is inadequate is that not all the model calculations are done spectrally. Most sub-grid-scale physical processes are parameterized and modeled in real space, and it is important, therefore, to have a spectral topography without detrimental artifacts in real space. Global least-squares optimality for the deviations of the spectral topography from the true topography is satisfied by the standard spectral expansion, but clearly this is insufficient to avoid Gibbs oscillations.

These problems have been recognized and two approaches have been proposed to deal with them. The first, explored by Navarra et al. (1994), uses various filters to smooth the topography either by what is essentially a convolution with a fixed kernel (Sardeshmukh and Hoskins 1984) or by smoothing selected locations directly in real space, which is equivalent to smoothing with a site-specific kernel. While this approach reduces Gibbs oscillations by smoothing sharp gradients, it does not control the choice of a site-specific kernel in some objective way, and a convolution with a fixed kernel will generally reduce maxima. Filters have the advantage of being numerically efficient so that they could be applied at every time step to a dynamical variable such as temperature and water vapor mixing ratio (Navarra et al. 1994), if one deems this to be physically acceptable.

The second approach, proposed by Bouteloup (1995), determines the spectral coefficients of the topography by minimizing a cost function that has a high penalty for nonflat oceans. This approach has great flexibility and generality and builds naturally on the least-squares optimality of the standard spectral topography. Constraints to preserve local maxima and any other desirable features can be built into the cost function. Although the cost function is arbitrary in form and must be artfully crafted, it is no more arbitrary than a choice of site-specific smoothing kernel. Once the cost function is chosen, the optimal-topography approach has the advantage of determining the spectral coefficients by applying a global criterion homogeneously and isotropically. The fact that minimizing a cost function is numerically more expensive than a filter is not an issue for the topographic height field whose spectral representation needs to be determined only once.

Corresponding author address: Dr. Mark Holzer, Canadian Centre for Climate Modelling and Analysis, Atmospheric Environment Service, University of Victoria, P.O. Box 1700, Victoria, BC V8W 2Y2 Canada.

In this paper, we build on the ideas of Bouteloup (1995) to obtain an optimal spectral topography for the Canadian Climate Centre (CCC) GCM (McFarlane et al. 1992). Our cost function depends not only on the topographic height but also on its gradients to efficiently alleviate Gibbs oscillations. In this sense, our approach amounts to optimal smoothing while enforcing local maxima by minimizing an appropriate global cost function.

In the following section we briefly define spectral topography and state its basic properties relevant to our purposes. We present our rationale for the choice of cost function and related issues in section 3. In section 4, we examine the sensitivity of the CCC GCM's climate to the switch from standard to optimal topography at T32 and T48 resolutions. We will show that the Gibbs oscillations in the standard spectral topography induce significant ripples in the surface fluxes. For example, the surface energy balance can have grid-scale oscillations of peak-to-peak amplitude $O(50 \text{ W m}^{-2})$. Such ripples are strongly suppressed in the climate with the optimal topography. It follows that an optimal topography with flat oceans is of importance to coupling atmospheric GCMs to ocean GCMs, where it will likely help keep flux corrections to a minimum.

2. Spectral topography and least-squares optimality

The height field of the spectral topography, Z^s, is defined as the truncated expansion in spherical harmonics

$$Z^s(\lambda, \mu) = \sum_{n=0}^{N} \sum_{m=-n}^{n} \tilde{Z}_n^m P_n^m(\mu) e^{im\lambda}, \quad (1)$$

where the $\tilde{Z}_n^m$ are the (complex) expansion coefficients, P_n^m is the associated Legendre function, and λ and $\mu \equiv \sin\phi$ are the longitude and sine of the latitude, ϕ, respectively. [The truncation of the spectral expansion used in (1) is referred to as triangular truncation at wavenumber $n = N$, or TN truncation or resolution.] Because Z^s is real, $\tilde{Z}_n^{-m} = (-1)^m \tilde{Z}_n^{m*}$, so that (1) contains $(N + 1)^2$ independent real expansion coefficients ("degrees of freedom"), and we may take the coefficients, $\tilde{Z}_n^m$, with $m \geq 0$, as independent.

Given the "true" topography, $Z(\lambda, \mu)$, specified on a $2N_0 \times N_0$ Gaussian grid (GG) (which consists of $2N_0$ equally spaced longitudes and N_0 latitudes corresponding to the zeros of $P_{N_0}^0$), with $N_0 \geq N$, the spectral coefficients are normally found via a discrete Fourier transform over the longitudes and via Gaussian quadrature, with weights $W_{N_0}(\mu)$, over latitudes:

$$\tilde{Z}_n^m = \sum_{\lambda,\mu \in GG} \frac{W_{N_0}(\mu)}{2N_0} Z(\lambda, \mu) P_n^m(\mu) e^{-im\lambda}. \quad (2)$$

It is easily shown that (1), with coefficients generated via the transform (2), is an optimal approximation to Z in the area-weighted least squares sense. More precisely, the cost function

$$\mathcal{E}(Z, Z^s) \equiv \sum_{\lambda,\mu \in GG} W_{N_0}(\mu) \left| \frac{Z - Z^s}{Z_0} \right|^\gamma, \quad (3)$$

for $\gamma = 2$, and Z^s given by (1), is minimized when the $\tilde{Z}_n^m$ are obtained via (2). Thus, if the $\tilde{Z}_n^m$ are determined from (2), Z^s is a least squares fit to Z. [In (3) Z_0 is a global constant to nondimensionalize the height field.]

3. Construction of a cost function and its optimal topography

The idea behind an optimal topography is to change the form of the cost function, $\mathcal{E}$, such that the Z^s that minimizes $\mathcal{E}$ is as nearly as possible free of Gibbs oscillations while preserving, as much as possible, local maxima. As in Bouteloup's approach, we will encode all geographic weighting of the cost function in the power γ and otherwise retain the functional form (3). However, unlike Bouteloup (1995), we include explicit dependence of γ on the gradients of Z since it is large gradients that are responsible for Gibbs oscillations. [Bouteloup chooses the form $\gamma = a + b \exp(-c|Z|)$, where a, b, and c are independent of the topography but can have some dependence on the coordinates and stretching parameter of a coordinate system centered on France.] To ensure local maxima are preserved as much as possible, our cost function also depends directly on Z scaled by its suitably defined local maxima.

To obtain an optimal spectral topography involves three main steps: (a) a decision regarding what we will take as the true topography and on which grid, (b) a sensible choice for the form of the cost function, and (c) minimization of the cost function. We will now deal with each of these in turn and then present the resulting optimal topographies for T48 and T32 resolutions. At the end of this section we will briefly revisit the choice of including the geographic weighting in the exponent.

a. Choice of grid and coarse-grained topography

Because the optimal spectral topography is essentially a least-$\mathcal{E}$ fit to what we specify as the "true," or "fitting," topography, this fitting topography should be a suitably coarse-grained version of the real continuous topography such that its height field represents an average over an area whose scale corresponds to the spectral truncation. Furthermore, the grid on which both the fitting and the spectral topography are evaluated must be sufficiently fine to sample any Gibbs oscillations since the difference $Z^s(\mathbf{x}) - Z(\mathbf{x})$, with $\mathbf{x}$ on this grid, enters the cost function.

Regarding the choice of grid, it should first be emphasized that the smallest GG that can represent a field with TN truncation, that is, the GG with $N_0 = N$, is not an equivalent grid in the sense that it and its spectral
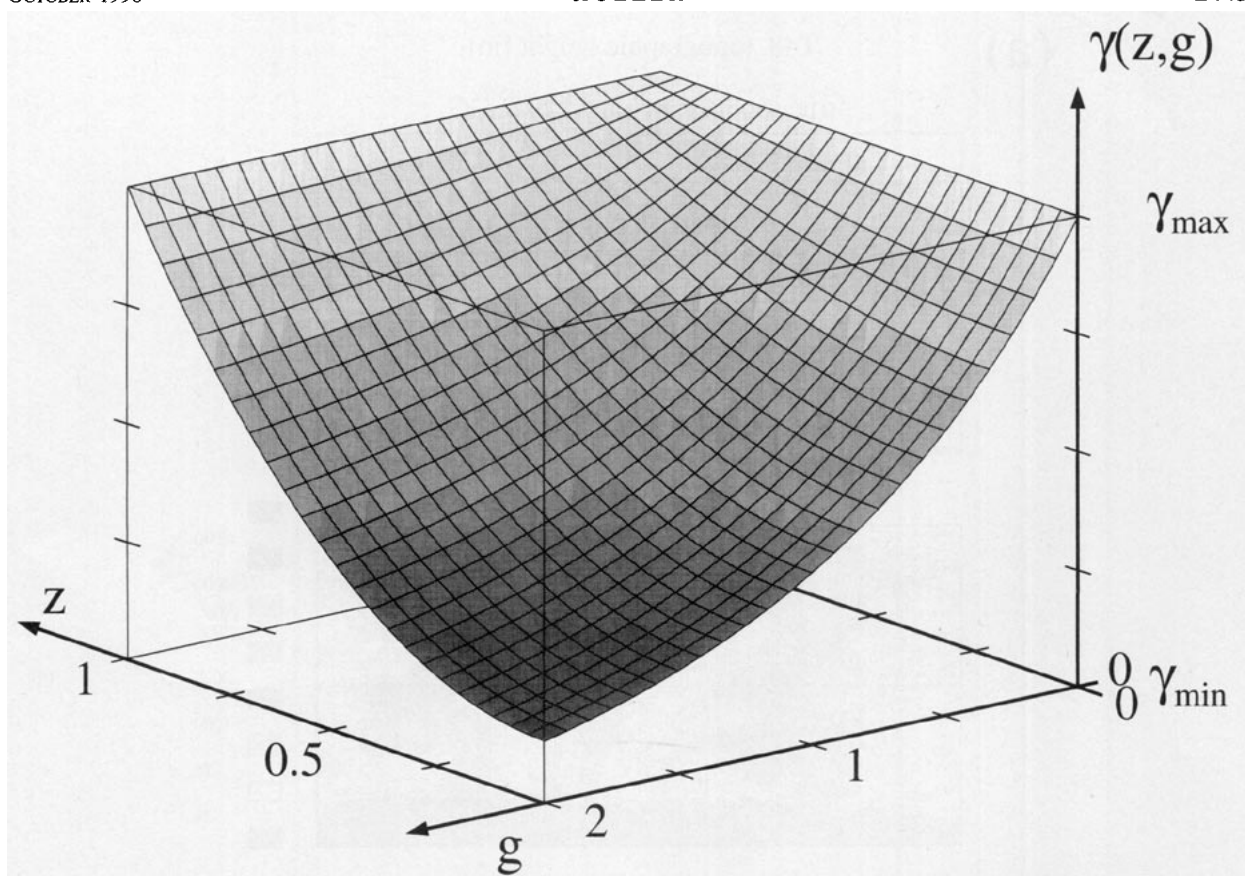
FIG. 1. The power $\gamma(z, g)$ of the cost function as a function of scaled height, z, and scaled gradient measure, g.

transform do not contain exactly the same information. [We refer to this grid as the "linear" GG to contrast with "quadratic" GG (see below).] The linear GG contains about twice the number of degrees of freedom as the corresponding spectral representation [$2N^2$ versus $(N + 1)^2$]. However, triangular truncation corresponds to the same resolved scale at any point on the globe by virtue of the symmetry invariances of spherical harmonics (see, e.g., Sardeshmukh and Hoskins 1984; Jackson 1975), so that this loss of information is desirable because the linear GG is overresolving especially and obviously at high latitudes.

Because even the linear grid overresolves the scales contained in the corresponding truncated spectral expansion, the Gibbs oscillations are evident already on this grid. (This contrasts with the discrete Fourier transform of doubly periodic data, which is one to one and represents the data on its equivalent grid exactly, so that Gibbs oscillations are seen only when evaluating the spectral expansion on a finer grid. It should be kept in mind, however, that even in this case gradients evaluated on the equivalent grid reveal any Gibbs oscillations. Thus, even if our spectral transform on the sphere were one to one, we would still need to worry about Gibbs oscillations.) Nevertheless, the linear GG only barely resolves

Gibbs oscillations close to the equator, and we choose a finer grid, namely, the $(3N \times 3N/2)$ GG. We will refer to this grid as the quadratic GG, as it is the grid on which the quadratic terms of the dynamics are dealiased. Also, this is the grid on which real-space parameterizations are evaluated in the current versions of the CCC GCM (McFarlane et al. 1992).

Our starting point for what we will take to be the true topography is the initial height field, Z_I, defined on the quadratic GG, which corresponds to an area-weighted average, over the associated grid box, of a high-resolution $1° \times 1°$ topography. [This $1° \times 1°$ topography was in turn obtained by area averaging a $10' \times 10'$ dataset from the U.S. Navy (Joseph 1980).] The standard spectral topography of the CCC GCM is the spectral transform (2) of Z_I. However, what is needed to fit the spectral topography in real space is a topography that has been coarse-grained in a homogeneous fashion, so that every height on the globe corresponds to an average over the *same* area. This is not the case for Z_I since the area averaged over becomes increasingly smaller at high latitudes. Hence, using Z_I in the minimization would potentially give the resulting Z^s a high bias at high latitudes. The desired homogeneously coarse-grained field could, for example, be obtained by

FIG. 2. (a) The topographies for T48. The "true" topography is the homogeneously re-coarse-grained "fitting" topography on the "quadratic" GG as described in the text and in appendix A. From −75 to +175 m, the contour interval is 50 m (straddling zero symmetrically). The other contours are at $n \times 1000$ m (integer n). (b) As in (a) but for T32. (For plotting purposes, all spectral topographies were evaluated on a 300 × 150 GG to smoothly sample any Gibbs oscillations.)

averaging the high-resolution data over a circular patch of constant solid angle at the earth's center. Here, however, we simply re-coarse-grain Z_l by performing an area-weighted average over a latitude–longitude box centered on each point of the GG with (approximately) constant latitudinal size and a longitudinal extent that is adjusted so that every such box has the same area, A_0. The area A_0 is chosen to be larger than the area, A_{max}, of an equatorial grid box of the quadratic GG because the distance between equatorial nearest neighbors of this GG is smaller by a factor of 3/2 than the nominal length scale of the associated spectral truncation. The ratio A_0/A_{max} is controlled by an adjustable nondimensional parameter, α, where $3/2 > \alpha > 1$ and $A_0/A_{max} \sim \alpha^2$. The precise details of the re-coarse-graining procedure are given in appendix A but should

FIG. 2. (*Continued*)

not be important as long as the fitting topography respects the homogeneity of triangular truncation.

b. Construction of cost function

To construct the cost function, we need an appropriate nondimensional measure, g, of the gradient of Z. As a simple positive-definite measure of the gradient we take

$$g(\mathbf{x}) \equiv \frac{1}{\zeta_0} \left\{ \frac{1}{4} \sum_{\Delta \in \{NN\}} \left[\frac{Z(\mathbf{x} + \Delta) - Z(\mathbf{x})}{d(\Delta)} \right]^2 \right\}^{1/2},$$

(4)

where $\mathbf{x}$ is a point of the quadratic GG, the sum is over its four nearest neighbors (NN), Δ is the displacement between $\mathbf{x}$ and its neighbor, $\mathbf{x} + \Delta$, $d(\Delta)$ is the geodesic distance between $\mathbf{x}$ and $\mathbf{x} + \Delta$, and ζ_0 is a global constant. We want a cost function that allows deviations of Z^s from Z in high-gradient regions and demands accuracy for local maxima in low-gradient regions such as the oceans. We nondimensionalize the height field by taking Z_0 to be 1 m so that almost everywhere $|Z - Z^s|/Z_0 \gg 1$. Thus, the larger the power γ in (3), the larger the cost in having Z and Z^s different by more than Z_0. We might, therefore, write

$$\gamma(g) = G[g(\mathbf{x})] \equiv \gamma_{min} + (\gamma_{max} - \gamma_{min})e^{-g(\mathbf{x})}, \quad (5)$$

so that $\gamma = \gamma_{min}$ for large g and $\gamma = \gamma_{max}$ for $g = 0$. However, inspection of $G(\mathbf{x})$ shows that throughout the interior of mountainous regions, the terrain is rough (large g) and hence $\gamma \sim \gamma_{min}$. This is not desirable because we wish to constrain the height field to have approximately correct local maxima. This can be accomplished by making $\gamma(\mathbf{x})$ also a function of $Z(\mathbf{x})$ rescaled by the maximum of Z in the neighborhood of $\mathbf{x}$.

We define the neighbourhood of a grid point by a patch of angular radius θ_0 as follows: if $\mathbf{x}$ is a radial vector from the center of the earth to the point of interest, $\mathbf{x}'$ is in its neighborhood if

$$\arccos\left(\frac{\mathbf{x} \cdot \mathbf{x}'}{|\mathbf{x}| |\mathbf{x}'|}\right) \leqslant \theta_0. \quad (6)$$

Typically, we take θ_0 to correspond to about twice the angular separation between points of the quadratic GG at the equator. The scaled height, $z(\mathbf{x})$, is now defined by

$$z(\mathbf{x}) \equiv \frac{Z(\mathbf{x})}{\eta_0 Z_{max}(\mathbf{x}, \theta_0)}, \quad (7)$$

where $Z_{max}(\mathbf{x}, \theta_0)$ denotes the maximum of Z in the patch of size θ_0 around $\mathbf{x}$, and $\eta_0 \geqslant 1$ is a $O(1)$ global scaling constant, so that $z(\mathbf{x}) \leqslant 1$.

With these choices for a gradient measure $g(\mathbf{x})$, and scaled height $z(\mathbf{x})$, we find that a satisfactory choice for γ is

$$\gamma(z, g) = G(g)[1 - F(z)] + \gamma_{max}F(z), \quad (8)$$

with $F(z) \equiv z^2$. The function $\gamma(z, g)$ defined by (8) smoothly connects $\gamma = G(g)$ at $z = 0$ with $\gamma = \gamma_{max}$ at $z = 1$ (i.e., $Z = \eta_0 Z_{max}$). The important, and we feel natural, feature of this choice for $\gamma(z, g)$ is its convex shape in the z-g plane such that high-gradient regions are low in cost if they do not coincide with close-to-local-maximum terrain (such as coast lines), and high in cost if they do, independent of g (see Fig. 1). The precise functional forms (i.e., exponential dependence on g and algebraic dependence on z) are probably not very important and presumably any other reasonable choice would also do.

It is clear that the construction of the cost function involves a number of arbitrary choices. The values of γ_{min} and γ_{max}, the grid over which the cost function is evaluated, the re-coarse-graining parameter α, and the functional form of the cost function itself are arbitrary and there is no physical principal to guide us. For the remainder of the paper we use the form (3) with (8) and $\gamma_{min} = 2$, $\gamma_{max} = 4$, and $Z_0 = 1$ m. The parameter Z_0 sets the scale for the difference between Z and Z^s. If $|Z - Z^s| > Z_0$, the larger γ, the higher the cost as desired. Thus, we want Z_0 to be small such that the reversed weighting (the larger γ, the lower the cost),

which occurs for $|Z - Z^s| < Z_0$, only comes into play when $|Z - Z^s|$ is already negligible. This is clearly the case for $Z_0 = 1$ m. We chose $\gamma_{min} = 2$, so that the cost of the "low cost" regions reduces to that of the (standard) quadratic cost function. The value of $\gamma_{max} = 4$ was determined as suitable after some experimentation; a much larger value leads the cost function to essentially ignore the quality of the fit where $\gamma_{min} = 2$. To determine α (see appendix A for definition), some experimentation showed $\alpha = 1.1$ to be acceptable independent of resolution. A larger value of α caused oversmoothing in the resulting "optimal" spectral topography. This leaves us with three adjustable parameters, η_0, ζ_0, and θ_0, which are static in the sense that they are held fixed during minimization. Since θ_0 is the only parameter that has an obvious dependence on horizontal resolution, we only adjust it according to the spectral truncation used. All other parameters have in principle no, or only weak, dependence on truncation.

c. Minimization of cost function

Finally, the cost function, $\mathcal{E}$, must be minimized in the $(N + 1)^2$-dimensional (real) space of the spectral coefficients to determine the optimal topography. The global minimum of $\mathcal{E}$ in this high-dimensional space could in principle be found via methods such as simulated annealing (see, e.g., Press et al. 1992, 436–448), but here we will be content with finding some well-defined minimum that has flat oceans and that is in a sense close to the standard spectral topography. Since the optimal topography should not be wildly different from the standard spectral topography, we initialize the spectral coefficients to those of the standard spectral topography. We then simply perform a "downgradient" minimization, which is periodically nudged to ensure the algorithm does not get stuck in the first available minimum. For the down gradient minimization, we use a truncated Newton method (Press et al. 1992), which makes use of the analytic form of $\partial\mathcal{E}/\partial\tilde{Z}_m^n$ (appendix B). The nudging is accomplished by periodically transforming the spectral coefficients to the quadratic GG, "clipping" off nonflat $Z^s(\mathbf{x})$ in high-cost regions of the oceans, transforming back, and continuing the minimization (for details, see appendix B). This nudging of the minimization may be thought of as a deterministic version of the random (Monte Carlo) exploration of parameter space in simulated annealing.

The nudged downgradient algorithm reduces $\mathcal{E}$ by about three orders of magnitude and converges to a minimum of $\mathcal{E}$, which has strongly reduced Gibbs oscillations and nearly flat oceans. We have, of course, no proof that our final state is close to the global minimum of $\mathcal{E}$ or that the global minimum has oceans as flat as our final state. (One could in principle imagine a global minimum with nearly perfect spectral topography everywhere, except for one delta function in the

middle of an ocean, although one hopes that our cost function is free of such pathologies.) Nevertheless, using a well-defined algorithm we find spectral coefficients that have the desired attributes and whose "cost," $\mathcal{E}$, is much less than that of the standard spectral topography.

To guide us in the choice of the static parameters (parameters of $\mathcal{E}$ other than the spectral coefficients), we considered as a scalar measure of merit the mean negative spectral topography $\langle Z^s \rangle^- \equiv \Sigma_{GG} \ W(\mu) Z^s \Theta(-Z^s) / \Sigma_{GG} \ W(\mu) \Theta(-Z^s)$, where the Heaviside function $\Theta(x) = 0$ if $x < 0$, and $\Theta(x) = 1$ otherwise. Clearly, $\langle Z^s \rangle^-$ is not necessarily minimized by the optimal topography, but the gradient of $\langle Z^s \rangle^-$ with respect to the static parameters gives some useful guidance.

d. Characterization of optimal topographies

Our best case of the T48 optimal spectral topography has static parameters $\eta_0 = 1.8$, $\zeta_0 = 1.611 \times 10^{-4}$, and $\theta_0 = 6°$ and is shown in Fig. 2a together with the standard spectral topography and the true (fitting) topography. To obtain a corresponding T32 optimal topography, we simply scale θ_0 by 48/32 to 9° and retain all other static parameters from the T48 case. The corresponding topographies for T32 are shown in Fig. 2b. In Fig. 2 areas where the topographic heights are below -75 m have been blackened to highlight the regions where the spectral topographies have Gibbs oscillations with particularly large amplitude. The peak-to-peak amplitude of the Gibbs oscillations of the standard spectral topographies can be as large as several hundred meters in the "trouble spots" off the coast of Greenland, south of the Himalayas, west of the Andes, and off the coast of Antarctica. On the quadratic GG, the T48 optimal spectral topography has only three grid points below -75 m, and these are no deeper than -80 m (off the Andes, in the Gulf of Mexico, in the Mediterranean). For the T32 optimal spectral topography (obtained without any further fine-tuning of static parameters), two grid points of the quadratic GG are below -75 m (-76 m off the east coast of Greenland, and -129 m in the Gulf of Mexico). The maxima of the earth's major mountainous regions as represented by the true, standard spectral, and optimal spectral topographies on the quadratic GG are compared in Table 1. Generally, the optimal spectral topography's maxima are closer to the true values, especially for the high, large-scale mountain systems.

In Fig. 3 we show zonal transects through the topographies at $\sim21°$S, where the Andes plunge into the Pacific, creating a near discontinuity and the worst Gibbs oscillations anywhere. Even in this region, the optimal topographies can be seen to have strongly suppressed Gibbs oscillations while preserving local maxima reasonably well. The figure shows both the T48 and T32 cases to illustrate that the Gibbs overshoot of the standard spectral topog-

TABLE 1. Comparison of the maxima of the earth's major mountainous regions. The spectral topographies, Z^s, are evaluated on the quadratic "fitting" grid on which the corresponding true topography, Z, is specified. The relative errors are defined as $(Z^s_{max} - Z_{max})/Z_{max}$.

	Regional topographic height maxima (m)				
Region	"True"	Standard,	% error	Optimal,	% error
		T32			
Andes	3517	3141	−11.0	3458	−1.7
Himalayas	5047	5638	12.0	5129	1.6
Rockies	2063	2192	6.3	2114	2.5
Ethiopian Highlands	1900	1714	−9.8	1777	−6.5
Greenland	2886	2960	2.6	2817	−2.4
Alps	982	821	−16.0	892	−9.2
Antarctica	3685	3863	4.8	3709	0.65
		T48			
Andes	3827	3514	−8.2	3636	−5.0
Himalayas	5263	5889	12.0	5374	2.1
Rockies	2384	2369	−0.63	2254	−5.5
Ethiopian Highlands	1967	2148	9.2	2004	1.9
Greenland	3028	3266	7.9	3178	5.0
Alps	1171	1061	−9.4	1071	−8.5
Antarctica	3825	3817	−0.21	3758	−1.8

raphy is not alleviated by going to moderately higher resolution. The main effect of increased resolution is that the wavelength of the oscillations is proportionately reduced. Correspondingly, there is a reduction in the area of the regions affected by Gibbs oscillations, although at T48, Gibbs "wave trains" traversing all the oceans are still visible at the ±25-m contour (Fig. 2a).

In Fig. 4, the spectra of the optimal topographies are compared with that of the standard spectral topography (which is close to the true spectrum, except for small corrections close to the truncation wavenumber due to the fact the Z_l is a coarse-grained representation of the continuous, real topography). Note that the spectra of the optimal topographies follow the true spectrum quite closely up to wavenumber $n_c \sim 20$ for T32, and $n_c \sim 30$ for T48, beyond which they decay more rapidly than the true spectrum as they must if the Gibbs oscillations are to be suppressed. The fact that the ratio $n_c(T48):n_c(T32)$ is about 48:32 indicates that our optimization procedure scales appropriately with system size.

Finally, we offer a few comments on whether we could have obtained the same "nonlinear" optimal spectral topographies, denoted for the moment by Z^s_ν, with a quadratic cost function $\mathcal{E}_Q = \Sigma_{GG} \ (W/Z^2_0)(Z^s - Z)^2 \Gamma$ that has spatially nonuniform weights Γ. A quadratic cost function has the advantage of having only one minimum that can easily be found by standard
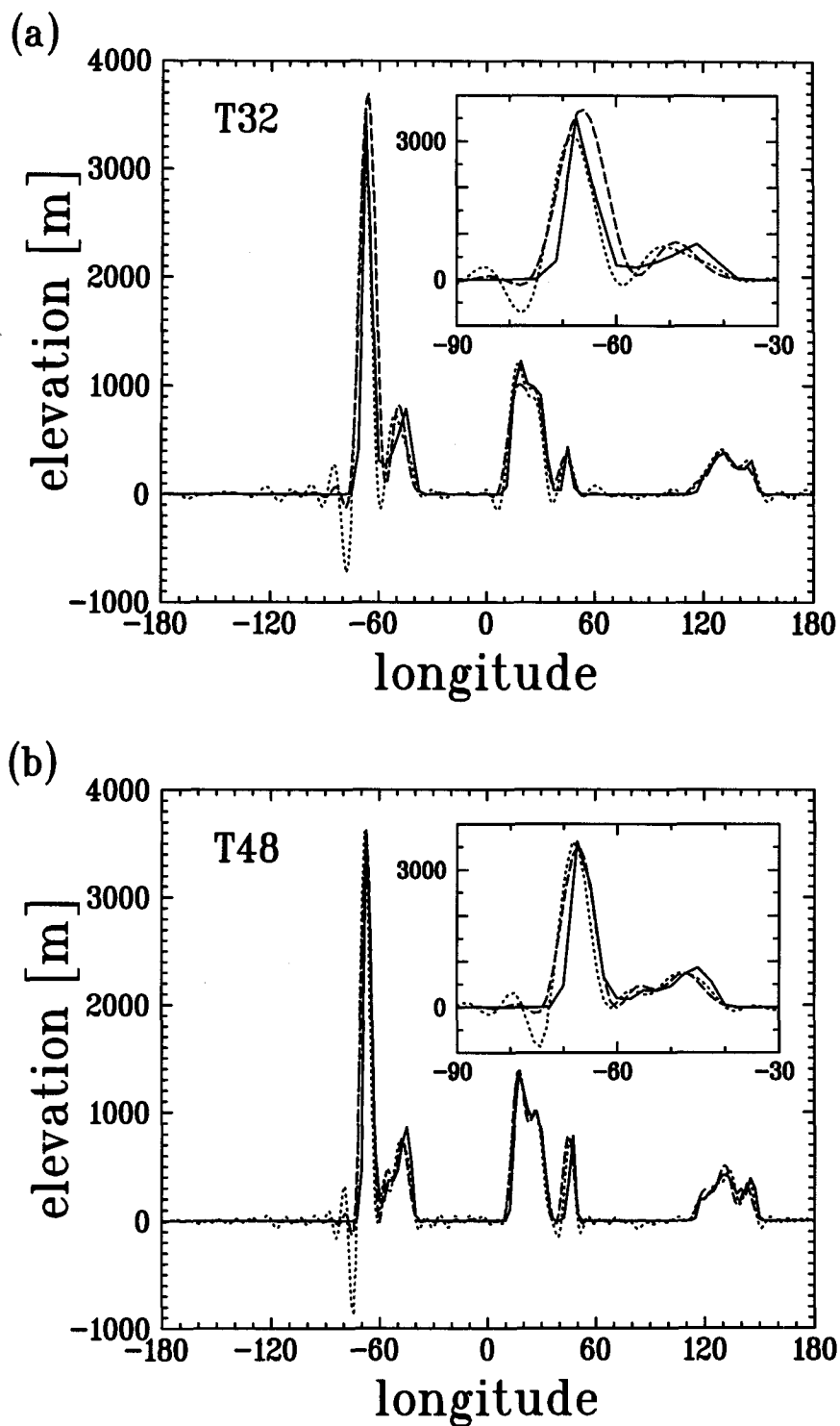
FIG. 3. Zonal slices through the topographies at ~21°S for T32 (a) and for T48 (b). The solid line is the (re-coarse-grained) "true" topography, the dotted line is the standard spectral topography, and the dashed line is the optimal spectral topography. The inset shows a blowup of the cut through South America.
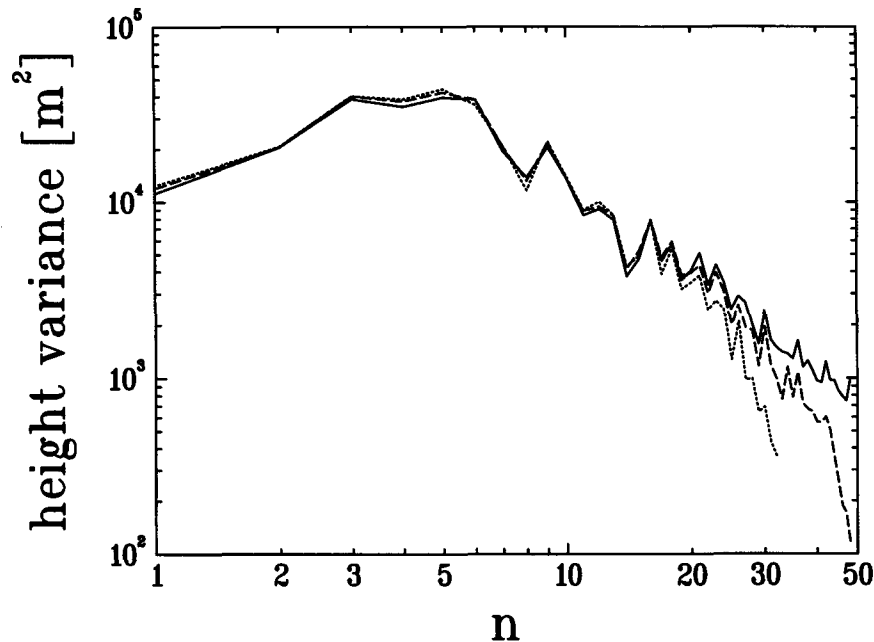
FIG. 4. Spectra of topographies $(\Sigma^n_{m=-n} |\tilde{Z}^m_n|^2$ as a function of n). The solid curve is for the standard spectral topography, the dashed (dotted) curve is for the T48 (T32) optimal spectral topography.

linear methods. For the minimum of $\mathcal{E}_Q$ to correspond to a *given* Z^s_ν, the weights Γ must satisfy $(\partial \mathcal{E}_Q/ \partial \tilde{Z}^n_m)|_{Z^s=Z^s_\nu} = 0$, which can be cast in matrix form as $\Sigma_x M_{k,x}\Gamma_x = 0$, where x labels points of the quadratic GG, and $k = (n, m)$ labels independent spectral coefficients. Thus, Γ must lie in the $[2(3N/2)^2 - (N + 1)^2]$-dimensional null space of M. However, since there are no simple constraints on the given Z^s_ν, there is no guarantee that this null space contains at least one vector Γ of all positive weights $[\Gamma(x) > 0$ for all $x]$. Therefore, in general it is not possible to find a positive definite $\mathcal{E}_Q$ whose minimum is identical to a given Z^s_ν. Of course, even if one could find a subspace of all positive weights, by working backward from a given Z^s_ν, it is not clear that one would be able to express at least one Γ as a simple function of z and g, which is clearly a prerequisite for a useful $\mathcal{E}_Q$.

Nevertheless, it may still be possible to get a good approximation to Z^s_ν with a quadratic cost function. Here, we simply note that using $\Gamma(z, g) = \gamma(z, g)$ as defined earlier, but with $\gamma_{min} = 1$, $\gamma_{max} = 100$, and $F(z) = z^4$, yields spectral topographies similar to the nonlinear ones, with strongly suppressed Gibbs oscillations and reasonable height maxima for T48, and with θ_0 scaled, also for T32. Although similar, these "linear" topographies are still inferior to those found from the nonquadratic cost function. Roughly, the few remaining spots where the topographic height is below -50 m (including those off the Andes) are two to three times deeper than those of the nonlinear optimal to-

pographies. For both T48 and T32, the maximum height of the Andes is $\sim$250 m below that of the corresponding nonlinear optimal topography, but the other height maxima of Table 1 are reproduced to within $\leqslant$50 m. The relative success of the functional form of the weights $\gamma(z, g)$ when used as the weights Γ of $\mathcal{E}_Q$ (without even any systematic exploration of static parameters) suggests that it is primarily the intuitive dependence of the weights on z and g that is responsible for suppressing Gibbs oscillations and ensuring adequate height maxima. Whether or not one uses these weights in the exponent or multiplicatively in $\mathcal{E}_Q$ appears to be of secondary importance.

4. Effects on model climate

To establish the effect of replacing the standard with the optimal spectral topography on model climate, we performed integrations with two versions of the CCC GCM. For T32, we use the single-transform version of the model ("GCMII," McFarlane et al. 1992) in which physical parameterizations are evaluated on the same grid as that used for the spectral transforms, namely the 96 $\times$ 48 quadratic GG. For T48, we use the double-transform version of the model (GCMIII) in which the parameterizations are evaluated on the 96 $\times$ 48 GG (the "physics grid") as before, but the spectral transforms are performed on a 144 $\times$ 72 GG (the quadratic GG for T48). Thus, for the T48 model, the resolved scale of the physics grid corresponds to the spectral

(a)   T48, mean sea-level pressure [mb]

DJF optimal

JJA optimal

DJF standard

JJA standard

DJF optimal-standard, 5% significance level
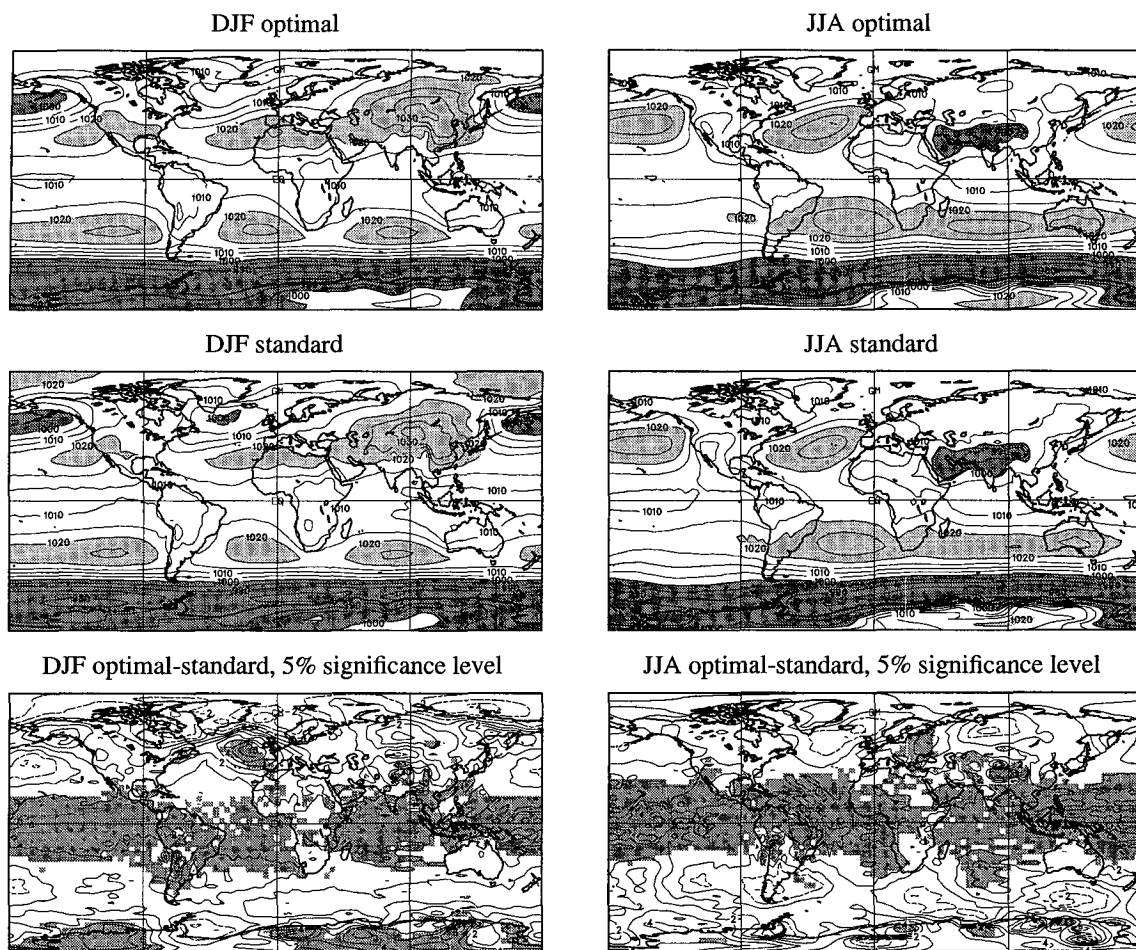
JJA optimal-standard, 5% significance level

FIG. 5. Maps of the mean sea level pressure for T48 (a) and T32 (b). The contour interval for the pressure maps is 5 mb, with dark shading below 1000 mb and light shading above 1020 mb. For the difference maps, the contour interval is 1 mb, and grid boxes for which

truncation at least at the equator. In addition to the increased horizontal resolution for the dynamics (T48), GCMIII also features higher vertical resolution (30 levels to 1 mb, versus 10 levels to 10 mb in GCMII), an improved land-surface scheme (Verseghy 1991; Verseghy et al. 1993), a penetrative convection parameterization (Zhang and McFarlane 1995), and a hybrid moisture variable to reduce "hole filling." {The hybrid moisture variable, s, is defined in terms of the specific humidity, q as $s = q$ for $q \geq q_0$, and $s = q_0/[1 - \ln(q/q_0)]$ for $q < q_0$, with $q_0 = 10$ g kg^{-1}.} For both T32 and T48, the fields shown in this section are evaluated on the 96 × 48 (physics) GG.

For summer (JJA) and winter (DJF), we compare the grand seasonal means, obtained with the optimal spectral topography (the "experiment"), with the grand seasonal means of the corresponding model with standard spectral topography (the "control").

For T48, we compare a 5-yr experiment with a 5-yr control, and for T32, a 3-yr experiment with a 10-yr control. [Such relatively short runs turn out to be sufficient to reveal statistically significant differences in the climates (see below).] Other than the difference in the spectral topographies, the models for experiment and control were identical and in particular used the same land mask and vegetation fields. In both the T32 and T48 cases, observed climatological sea surface temperatures (SSTs) were specified (annual cycle but no interannual variability). Differences (experiment − control, i.e., optimal − standard) in the grand seasonal means of some quantity X, denoted by δX, are tested for statistical significance with a t test based on the interannual variance of the seasonal means. (Unless explicitly stated otherwise, all variables in this section denote grand seasonal means; no overbar is used.)

(b)   T32, mean sea-level pressure [mb]

DJF optimal   JJA optimal

DJF standard   JJA standard

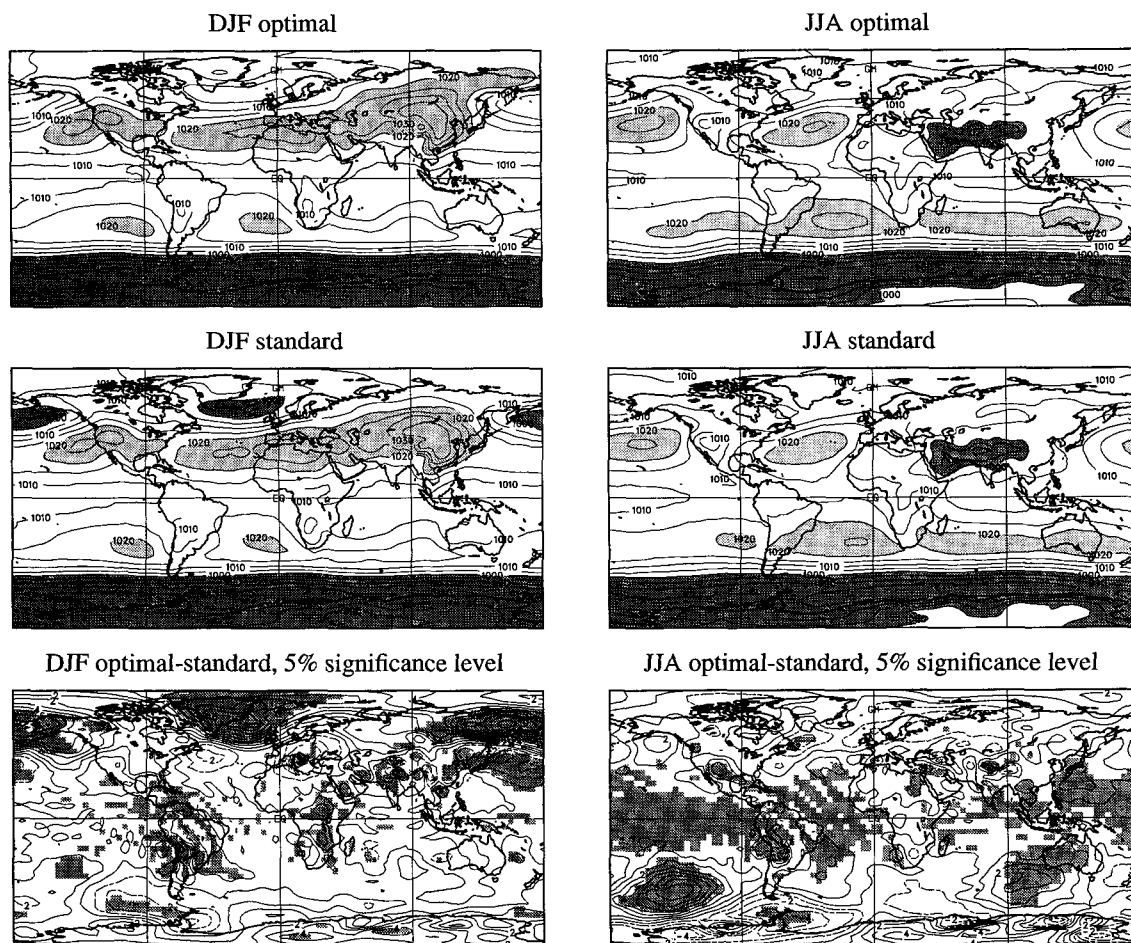DJF optimal-standard, 5% significance level   JJA optimal-standard, 5% significance level

FIG. 5. (Continued) the difference of means is statistically significant at the 5% level are shaded.

For both the T48 and T32 climates, zonally averaged quantities do not differ significantly between experiment and control. There are only relatively small differences in the large-scale fields of which those in the mean-sea-level pressure (MSLP), shown below, are typical. The most pronounced, statistically significant changes are evident in the surface fluxes and stresses that will be the main focus of this section.

Figures 5a–b show MSLP for DJF and JJA. For T48 (Fig. 5a), there are only minor differences in MSLP between the standard and optimal topographies. Increases of $O(1 \text{ mb})$ in the Tropics are statistically significant at the 5% level due to the small variability of the sea level pressure in the Tropics. For DJF, there is also a statistically significant change over the eastern north Atlantic off Europe, where the optimal case has a slightly higher Icelandic low and slightly stronger ridge over Europe. For T32 (Fig. 5b), the optimal topography shows improvements in MSLP for DJF in the

Northern Hemisphere. The Aleutian low does not penetrate as far inland as in the standard case. This is presumably due to the flatter Gulf of Alaska, and the fact that the Alaskan mountains of the optimal spectral topography extend farther west (see Fig. 2b), giving a better representation of the blocking effect of the Alaskan coastal range. The Aleutian low is also not as deep and allows the east Asian high to extend over Siberia, in closer agreement with observations. The statistically significant change over the north Atlantic corresponds to a higher Icelandic low in the optimal case, which is somewhat closer to observations. For JJA, the statistically significant differences are again small changes in the Tropics and a slight enhancement and westward extension of the South Pacific subtropical high.

Ripples in the standard spectral topography over the oceans do not produce rainbands directly through spurious orographic lift. However, when precipitation, P, is large, such as during the Indian summer monsoon,

δP shows a clear correlation with the topographic ripples δZ^s (Figs. 6a–b). Where grid-scale bumps in the ocean are flattened there is less precipitation, where depressions are raised there is more. The major "rainbands" in δP, especially for T48 over the Bay of Bengal (Fig. 6a), are statistically significant at the 5% level. Although both optimal and standard topographies represent India as a single mountain at T32 resolution, the flatter oceans of the optimal topography come at the price of more circular topography contours. Nevertheless, a flatter Arabian Sea, together with a slightly higher terrain over central western India, conspire to give a more realistic precipitation field in the T32 optimal case, which has a well-defined maximum in P of ~ 9 mm day^{-1} over western India (Fig. 6b). The standard case has a maximum in P of more realistic elongated shape, but it is too low by a factor of about 2. An atlas (e.g., Fullard and Darby 1984, 89) shows a maximum of P along the Western Ghats mountain range in excess of ~ 12 mm day^{-1} over an area roughly equivalent to that enclosed by the 8 mm day^{-1} contour of the T32 optimal case. At T48 resolution there are no significant differences over the Western Ghats, but δP and the fields themselves clearly show that the precipitation from the standard run has a high-wavenumber spatial modulation on the order of ~ 2 mm day^{-1}, which is correlated with the spurious Gibbs ripples.

The fluxes that couple the atmosphere to the ocean are the freshwater flux $P - E$ (where E is the surface evaporation flux), the wind stress, τ, exerted on the surface, and the net energy balance at the surface, H_G. We briefly examine the general features of these fields and then focus more closely on a representative feature of δH_G, which shows a particularly large response to δZ^s. Figure 7 shows that $P - E$ is smoother for the run with the optimal topography, and especially for T48, conspicuous ripples in the south Pacific visible for the standard run are absent. (The covariance of $P \times E$ was not available to allow computation of a statistical significance level.) The response of the wind stress, $\delta \tau$, to having Gibbs ripples nearly eliminated is shown in Fig. 8. (The grand-seasonal-mean value of the stress amplitude was estimated as the amplitude of the mean stress, i.e., $|\overline{\tau}| \sim |\overline{\tau}|$.) Ripples in $\delta|\tau|$ are clearly aligned with ripples in δZ^s (Fig. 2), where $\delta \tau$ is statistically significant (at the 10% and 2% levels of a Hotelling t test for vectors).

Figures 9a–b show the net energy balance at the surface, H_G. For the standard topography, large-amplitude ripples in H_G can be seen over the oceans. For T48 (Fig. 9a), H_G shows a pronounced wave train from the Andes to the central tropical Pacific, where $\delta H_G/H_G$ can exceed 50% with both H_G and δH_G on the order of several tens of watts per square meter (Fig. 10, middle and fourth panel). For T32 (Fig. 9b), the Pacific feature is less pronounced, but there are large-amplitude ripples in H_G stretching across the tropical Atlantic from northeast South America to northwest Africa. For

both T32 and T48, these ripples align with corresponding features in the standard topography (Fig. 2) and in $\delta|\tau|$ (Fig. 8).

We focused on the region (45°S–45°N) × (180°–GM) for τ and H_G to show the details of a response to δZ^s with large signal to noise ratio (~ 5–10) and hence large t-ratio. (For a response δX, we define the signal to noise ratio as $|\delta X|/\sigma_X$, where σ_X^2 is the interannual variance of X.) Both fields also exhibit a "spotty" band of statistically significant response with comparable signal to noise ratio just off the coast of Antarctica (not shown). The Gibbs ripples, δZ^s, in this region are also large and align with the response much as they do for the Pacific feature.

As a quantitative measure of the correlation between the differences of some field, δX, and the change in the spectral topography, δZ^s, we compute the area-averaged correlation coefficient, r, defined as

$$r \equiv \frac{\langle \delta X' \delta Z^{s'} \rangle}{[\langle (\delta X')^2 \rangle \langle (\delta Z^{s'})^2 \rangle]^{1/2}}, \quad (9)$$

where $\langle \ \rangle$ denotes the spatial average over the area of interest, $\delta X' \equiv \delta X - \langle \delta X \rangle$, and $\delta Z^{s'} \equiv \delta Z^s - \langle \delta Z^s \rangle$. For T48, these correlation coefficients are collected in Table 2 for a number of surface fields, where the areas of interest are the entire globe, land only, ocean only, and those parts of the ocean where δX is statistically significant at the 5% level. [When X is a vector magnitude, $|V|$, the regions where δV (not $\delta|V|$) is significant at the 5% level are used to define "ocean and 5%".] Because the t test at the 5% level selects regions of high signal to noise ratio, the "ocean and 5%" correlations are much higher than the oceanwide ones. The best-correlated field listed in Table 2 is the temperature at the lowest model level, T_L. This is no surprise over land, where (anti)correlations exceed -0.75, since higher land sees lower ambient pressure and hence cooler atmospheric temperatures with which the land surface is allowed to equilibrate. The relatively high (anti)correlations over the oceans are less obvious because the SSTs are identical between experiment and control. Nevertheless, changes in elevation imply changes in the ambient pressure that are sufficient to change the average air temperature at the lowest level. However, there is substantial control by the SSTs through heating as can be seen, for example, from the fact that δT_L over the oceans is much less than what would be expected from δZ^s if one was merely seeing an adiabatic lapse rate (Fig. 10, second panel).

We now focus on the ripples of H_G in the Pacific for T48 and ask through which basic physical processes the Gibbs oscillations in the sea surface height induce modulations in H_G. The surface energy balance is defined by

$$H_G \equiv -LE - H + R$$

$$+ \text{(other phase change terms)}, \quad (10)$$

FIG. 6. Maps of the JJA Indian monsoon precipitation for the area (5°S–30°N) × (60°–120°E) for T48 (a) and T32 (b). The contour interval of the precipitation itself is 2 mm day^{-1}. The difference field is contoured every 1 mm day^{-1} and overlaid with shaded grid boxes where the difference of means is statistically significant at the 5% level. For reference, the difference field, δZ^s, of the spectral topographic height is shown with a contour interval of 50 m (light shading for $\delta Z^s > 25$ m; dark shading for $\delta Z^s < -25$ m).

FIG. 7. The net freshwater flux into the surface, $P - E$, with a contour interval of 1 mm day^{-1}. The largest value contoured is 6 mm day^{-1}.

where LE is the latent heat flux due to evaporation, H is the sensible heat flux into the atmosphere, and R is the surface radiation balance. In the Tropics freezing of water at the surface is unlikely, so that

$$\delta H_G = -L\delta E - \delta H + \delta R. \qquad (11)$$

Because both experiment and control were forced with identical SSTs, there is no change in the outgoing long-wave radiation and δR represents changes in the absorbed incoming radiation flux only. Figure 10 (fourth panel) shows the balance (11). The ripples in δR are consistent with ripples in the total cloud fraction, δC (not shown). Over the region under discussion, δC has a peak-to-peak amplitude of ~15%. (Although there is no perfect correlation, generally more clouds result in less absorbed solar radiation at the surface, that is, δR ~ $-\delta C$.) We will now focus on the latent heat term $L\delta E$, which is seen to dominate the surface energy balance.

The evaporation flux, E, is parameterized in the GCM as

$$E = -\rho C(\text{Ri})|\mathbf{v}|(q - q^*), \qquad (12)$$

where $C(\text{Ri})$ is a turbulent transport coefficient pa-

rameterized as a function of a bulk Richardson number, Ri; the quantities ρ, $|\mathbf{v}|$, and q are the air density, wind speed, and specific humidity at the lowest model level; and q^* is the saturation specific humidity at the surface. In (12) only, all variables denote quasi-instantaneous quantities (adjusted at each time step of the model) and not grand-seasonal means like elsewhere in this section. We have checked from daily data that, to a reasonable approximation, a similar equation holds for the grand-seasonal means so that we may write

$$E \sim -\hat{C}|\mathbf{v}|Q, \qquad (13)$$

where $Q \equiv (q - q^*)$ and $\hat{C}$ is approximately constant ($\Delta\hat{C}/\hat{C} \sim 5\%$ in the region of interest). Thus, it follows that

$$\frac{\delta E}{E} \sim \frac{\delta|\mathbf{v}|}{|\mathbf{v}|} + \frac{\delta Q}{Q}. \qquad (14)$$

This is not a precise equality because of the neglect of $\delta\delta$ second-order terms and also because (13) neglects temporal correlations between the various terms of (12).

We can use (14) to get a qualitative idea of how the induced changes in the wind and moisture fields con-

FIG. 8. The difference in the wind stress, $\delta\tau$, (vectors) over the ocean for the area (45°S–45°N) × (180°–GM). In the top panels the shading indicates $\delta|\tau|$. In the bottom panels grid boxes are shaded where $\delta\tau$ is statistically significant.

tribute to the large induced changes in the surface energy balance. [This is similar in spirit to the work of Boer (1993), who studied climate changes induced by a doubling of CO_2.] Figure 10 (bottom panel) shows that $\delta|\mathbf{v}|/|\mathbf{v}|$ and $\delta Q/Q$ have the same sign and contribute roughly equally to the ripple feature of δH_G in the Pacific. [The denominators in (14) are taken from the climate with the optimal topography and do not go through zero in the region of interest (see Fig. 10, middle panel).] The signs of δQ and $\delta|\mathbf{v}|$ make intuitive sense and are consistent with δT_L shown in Fig. 10: cooler (warmer) overlying air is drier (more moist), causing a larger (smaller) vertical surface moisture gradient, Q. One also expects flow to speed up over the crests of Gibbs ripples and to slow down over troughs, giving the sign of $\delta|\mathbf{v}|$ seen in Fig. 10 and in Table 2.

Finally, it is clear that not all topographic ripples induce observable ripples in the surface climatology. A number of factors must conspire to give a clean ripple response to δZ^s. For time series of only finite length, the response

will be most apparent where it is large compared to the interannual variability. Also, fields that are sensitive to the high-wavenumber topography, for example, precipitation and lowest-level temperature, T_L, over land, appear to have a larger, more direct, response to δZ^s than less sensitive large-scale fields like, for example, MSLP. From the analysis of the contribution of $\delta|\mathbf{v}|$ to δH_G (Fig. 10), it is also clear that modulations of the lowest-level wind can play an important role. Since $\delta|\mathbf{v}|$ is largest where the lowest-level wind is blowing across the ripples of the standard topography (i.e., in a direction perpendicular to the ripple crests), the largest ripple response in δH_G is expected from those wave trains of δZ^s that align with a strong surface circulation. This is consistent with the ripple features of δH_G in the Pacific for T48 and in the tropical Atlantic for T32.

5. Summary and conclusions

We have constructed a global cost function for the difference between the spectral and true topographies,

FIG. 9. Maps of the surface energy balance, H_G, for the area (45°S–45°N) × (180°–GM) for T48 (a) and T32 (b). The contour interval for H_G is 20 W m^{-2} with dark shading for $H_G < -80$ W m^{-2} and light shading for $H_G > 80$ W m^{-2}. Here δH_G is contoured with a 10 W m^{-2} interval, and grid boxes have been shaded where δH_G is statistically significant at the 5% level.

which when minimized largely eliminates Gibbs oscillations in the spectral topography, while preserving the large-scale height spectrum. The geographic weighting of the cost function is encoded in an exponent that depends on the true topographic height and a measure of its gradient. The weighting penalizes discrepancies from flatness over the ocean and tries to retain local maxima in the topography but is lenient in regions of large gradients that are the cause of Gibbs oscillations.

The Gibbs oscillations of the standard topography cause spurious ripples in the surface fields, particularly over the oceans. These ripples can extend over large

FIG. 9. (*Continued*)

regions (e.g., most of the tropical Atlantic and eastern tropical Pacific), have a wavelength on the order of two (equatorial) grid spacings, and, for the surface energy balance H_G, can have amplitudes as high as several tens of watts per square meter. The climates with the optimal topographies are nearly free of such ripples and have generally much smoother surface fluxes. The zonally averaged and large-scale fields of the climate with the standard topography are largely preserved in the corresponding optimal case.

Although the ripples of the standard topography over the ocean were not of sufficient amplitude to induce spurious rainbands as such, they do impose a spurious large-wavenumber modulation on the seasonal-mean precipitation. This modulation is particularly large and statis-
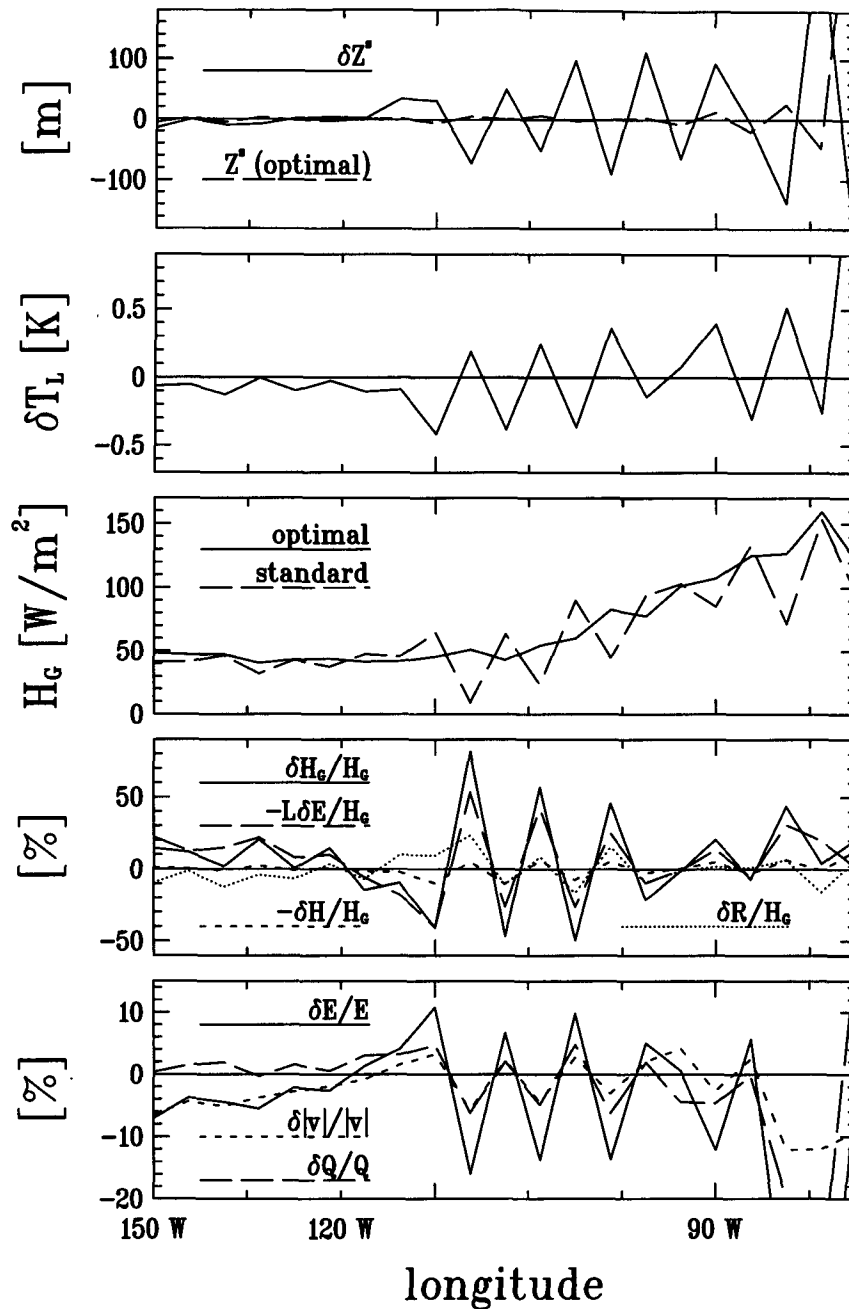
FIG. 10. Zonal slices through the fields indicated at $\sim 16.7°S$ (five grid boxes south of the equator on the 96 × 48 GG).

tically significant where both δZ^s and the precipitation are large, such as in the region of the Indian summer monsoon.

The large-amplitude ripple feature of H_G in the Pacific for T48 was examined in some detail. There δH_G is dominated by changes in the latent heat flux of evaporation $L\delta E$. Modulations in the lowest-level wind speed, $\delta|v|/|v|$, and in the vertical moisture gradient

at the surface, $\delta Q/Q$, each contribute about 50% to $\delta E/E$. The changes δQ are consistent with the changes in the lowest-level temperature, δT_L, which are anticorrelated with δZ^s as expected from adiabatic cooling over ripple crests.

Since the climate with the optimal topography is free of the large-amplitude, high-wavenumber spurious oscillations in the surface fluxes over the oceans, the op-

TABLE 2. Area-averaged correlation coefficients, r, defined by Eq. (9), for the correlation between the fields indicated and the change in height of the spectral topography, δZ^s. Here H_G is the surface energy balance, H is the sensible heat flux into the atmosphere, E is the evaporation flux, P is the precipitation flux, T_L is the lowest-level temperature, $|\mathbf{v}|$ is the lowest-level wind speed, and $|\tau|$ is the wind-stress amplitude. [The $P \times E$ covariance was not available to compute the 5% significance level for $\delta (P - E)$.]

Field	Global	Land only	Ocean only	Ocean and 5%
		JJA		
δH_G	−0.22	−0.03	−0.47	−0.63
δH	−0.23	−0.38	0.36	0.54
δE	0.30	0.30	0.41	0.59
δP	0.31	0.27	0.42	0.59
$\delta (P - E)$	0.18	0.18	0.19	—
δT_L	−0.69	−0.78	−0.40	−0.60
$\delta|\mathbf{v}|$	0.15	0.19	0.22	0.30
$\delta|\tau|$	0.08	0.10	0.20	0.26
		DJF		
δH_G	−0.20	0.05	−0.43	−0.54
δH	0.30	0.37	0.35	0.46
δE	−0.21	−0.40	0.36	0.46
δP	0.39	0.40	0.39	0.59
$\delta (P - E)$	0.29	0.34	0.19	—
δT_L	−0.69	−0.76	−0.41	−0.56
$\delta|\mathbf{v}|$	0.07	−0.01	0.14	0.10
$\delta|\tau|$	−0.10	−0.23	0.08	0.05

timal topography should be a definite asset when coupling an atmospheric GCM to an ocean model, possibly reducing local flux corrections.

APPENDIX A

Details of the Re-Coarse-Graining Procedure

The "initial" topography, Z_I, is re-coarse-grained as follows: we erect a latitude–longitude box of area A_0 and sides $\Delta\phi_j$ and $\Delta\lambda_j$ centered on each point (λ_i, ϕ_j) of the GG as shown in Fig. A1 (j labels latitudes and $\Delta\lambda_j$ depends only on latitude). Because the distance between equatorial nearest neighbors of the quadratic GG is smaller by a factor of $3/2$ than the nominal length scale of the associated spectral truncation, we take $A_0 > A_{max}$, where $A_{max}(\Delta\phi_{j0}, \Delta\lambda_{j0})$ is the area of the $\Delta\phi_{j0}$ by $\Delta\lambda_{j0}$ grid box of the GG at the equator (Fig. A1). We control the size of A_0 with the (adjustable, but glob-

ally constant) parameter α, with which we inflate the latitudinal grid spacing of the GG. Away from the poles, we take $\Delta\phi_j = \alpha\Delta\phi_j^{GG}$, where $\Delta\phi_j^{GG} \equiv (\phi_{j+1} + \phi_{j-1})/2$ is the latitudinal size of the GG box at latitude ϕ_j. (At the North Pole we use $\Delta\phi_{j_p} = \pi/2 - [\phi_j - \alpha(\phi_j - \phi_{j-1})/2]$, with a corresponding expression for the South Pole.) The longitudinal size, $\Delta\lambda_j$, of the re-coarse-graining box is then adjusted such that every such box has area $A_0 \equiv A_{max}(\alpha\Delta\phi_{j0}, \alpha\Delta\lambda_{j0})$. Thus, $A_0/A_{max} = \alpha \sin(\alpha\Delta\phi_{j0}/2)/\sin(\Delta\phi_{j0}/2) \sim \alpha^2$, where the approximation would be an equality if we were not on a sphere.

If the GG grid box associated with any $Z_I(\lambda_{i'}, \phi_{j'})$, has an overlap of area $A_{i,j;i',j'}$ with the re-coarse-graining grid box of area A_0 centered on (λ_i, ϕ_j), we define the re-coarse-grained height $Z(\lambda_i, \phi_j)$ by the area-weighted average

$$Z(\lambda_i, \phi_j) = \frac{1}{A_0} \sum_{i',j'} A_{i,j;i',j'} Z_I(\lambda_{i'}, \phi_{j'}), \quad (A1)$$

where $\sum_{i',j'} A_{i,j;i',j'} = A_0$.

The algorithm that produces Z_I from high-resolution datasets $Z_I = 0$ over ocean grid points, as determined from an independently computed land-mask on the quadratic GG. To make Z also consistent with this constraint, we simply set $Z = Z_I$ wherever $Z_I \leq 1$ m.

APPENDIX B

Details of Minimization and Clipping Algorithm

The truncated Newton algorithm used [a variant of the Davidon–Fletcher–Powell algorithm, see Press et al. (1992, 421), main routine DFPMIN] converges for a quadratic cost function of K degrees of freedom in K steps, which gives a scale for the number of steps necessary in the nonlinear case. The algorithm takes advantage of the fact that we know the analytic form of the gradients of the cost function, $\mathcal{E}$, with respect to the spectral coefficients. If x_n^m and y_n^m denote the real and imaginary parts of the *independent* ($m \geq 0$) coefficients $\tilde{Z}_n^m = x_n^m + iy_n^m$ (recall, $y_n^0 = 0$), these gradients are given by

$$\left(\frac{\partial\mathcal{E}}{\partial x_n^m}, \frac{\partial\mathcal{E}}{\partial y_n^m} \right)$$

$$= \sum_{GG} \frac{W\gamma}{Z_0} \left| \frac{Z^s - Z}{Z_0} \right|^{\gamma-2} \left(\frac{Z^s - Z}{Z_0} \right) \left(\frac{\partial Z^s}{\partial x_n^m}, \frac{\partial Z^s}{\partial y_n^m} \right),$$

$$(B1)$$

with

$$\frac{\partial Z^s}{\partial x_n^0} = P_n^0(\mu), \quad (B2)$$

and, for $m \neq 0$,

$$\left(\frac{\partial Z^s}{\partial x_n^m}, \frac{\partial Z^s}{\partial y_n^m}\right) = 2P_n^m(\mu)(\cos(m\lambda), -\sin(m\lambda)).$$

(B3)

To ensure that the downgradient minimization algorithm does not get stuck in the first local minimum it finds if other lower-cost minima are close by, we nudge the spectral coefficients periodically to steer the minimization toward a minimum (hopefully close to the global minimum) that has flat oceans and as little excess negative topographic height as possible. The nudging consists of periodically "clipping" off ripples over the ocean and any excess negative height as follows: every $O(N^2/5)$ steps of the truncated Newton algorithm, we transform to the quadratic GG and set $Z^s(\mathbf{x})$ to $Z(\mathbf{x})$ if $Z^s(\mathbf{x}) < 0$ anywhere, or if both $|Z(\mathbf{x})| < Z_0$ and $\gamma(\mathbf{x}) > \gamma_0$, with $\gamma_0 = 0.995\gamma_{max}$. This sets Z^s to Z over those regions of the oceans where we insist on a good fit (e.g., away from high-gradient coast lines) and over any regions where the spectral topography is negative. After the clipping, we transform back to spectral space and multiply $\tilde{Z}_0^0$ by a con-

stant to ensure the global mean height before and after the clipping is the same. (If this rescaling is not done, the clipping can shift the mean height, and the ensuing minimization, the large scales of the spectrum, by as much as a few meters per clip.)

The nudged minimization converges after $\sim 5N^2$ steps and reduces $\mathcal{E}$ by about three orders of magnitude when the standard spectral topography is used as the initial state. During the final stages of the algorithm, a clipping typically increases $\mathcal{E}$ by a factor of only ≤ 1.2, and the subsequent truncated Newton method appears to find approximately the same state that was obtained before the clipping. Whether our final state is clipped or not makes a negligible difference to the "optimal" spectral topography compared to the improvement already achieved over the standard spectral topography [over the oceans, $O(10 \text{ m})$ changes at a few grid points].

One might ask how effective the clipping is by itself in reducing Gibbs oscillations. A single clip reduces the amplitude of the Gibbs oscillations off the Andes by about a factor of two and lowers the cost, $\mathcal{E}$, by about an order of magnitude. Iterating the clipping (without any downhill minimization) converges to a "clipping
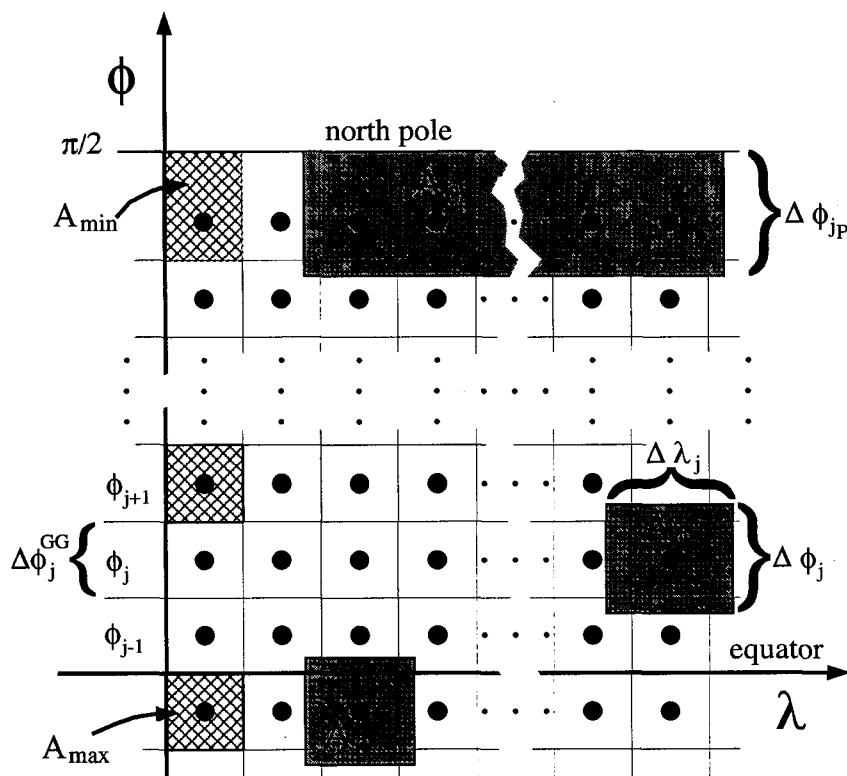

FIG. A1. Diagram explaining the various grid boxes discussed in appendix A. The heavy dots indicate the latitude–longitude quadratic GG. The cross-hatched areas are examples of the associated grid boxes. The grey-shaded areas are constructed to all have area $A_0 \sim \alpha^2 A_{max}$ and correspond to the areas over which the "initial" topography on the quadratic GG, Z_I, is averaged (with area weights) to form the "true," or "fitting," topography, Z, defined on the same GG.

topography'' that has a cost $\mathcal{E}$ reduced by about two orders of magnitude from that of the standard spectral topography. Over the oceans, the clipping topography turns out to be very close to that of the optimal topography. However, over land the clipping topography is very much degraded compared to both the standard and optimal topographies. For example, the local maximum over South America is significantly reduced (by ~ 1000 m), and obvious Gibbs oscillations over land (e.g., north of the Himalayas) are still present. The clipping by itself is thus not a viable means of reducing Gibbs oscillations without doing serious damage to the topography over land.

REFERENCES

Boer, G. J., 1993: Climate change and the regulation of the surface moisture and energy budgets. *Climate Dyn.*, **8**, 225–239.

Bouteloup, Y., 1995: Improvement of the spectral representation of the earth topography with a variational method. *Mon. Wea. Rev.*, **123**, 1560–1573.

Fullard, H., and H. C. Darby, 1984: *The Prentice-Hall University Atlas.* Prentice-Hall, 140 pp.

Jackson, J. D., 1975: *Classical Electrodynamics.* 2d ed. Wiley and Sons, 848 pp.

Joseph, D., 1980: Navy 10' global elevation values. NCAR Research Notes on the FNWC Terrain Data Set, 3 pp. [Available from NCAR Scientific Computing Division, Data Support Section, P.O. Box 3000, Boulder, CO 80307.]

McFarlane, N. A., G. J. Boer, J.-P. Blanchet, and M. Lazare, 1992: The Canadian Climate Centre second generation general circulation model and its equilibrium climate. *J. Climate,* **5**, 1013–1044.

Morse, P. M., and H. Feshbach, 1953: *Methods of Theoretical Physics.* McGraw-Hill, 997 pp.

Navarra, A., W. F. Stern, and K. Miyakoda, 1994: Reduction of the Gibbs oscillations in spectral model simulations. *J. Climate,* **7**, 1169–1183.

Press, W. H., S. A. Teukolsky, W. T. Vetterling, and B. P. Flannery, 1992: *Numerical Recipes.* 2d ed. Cambridge, 963 pp.

Sardeshmukh, P. D., and B. J. Hoskins, 1984: Spatial smoothing on the sphere. *Mon. Wea. Rev.,* **112**, 2524–2529.

Verseghy, D. L., 1991: CLASS—A Canadian land surface scheme for GCMs. Part I: Soil model. *Int. J. Climatol.,* **11**, 111–133.

——, N. A. McFarlane, and M. Lazare, 1993: CLASS—A Canadian land surface scheme for GCMs. Part II: Vegetation model and coupled runs. *Int. J. Climatol.,* **13**, 347–370.

Zhang, G. J., and N. A. McFarlane, 1995: Sensitivity of climate simulations to the parameterization of cumulus convection in the Canadian Climate Centre general circulation model. *Atmos.-Ocean.,* **33**, 407–446.